

RESEARCH ARTICLE

Discovery and inversion of the viscoelastic wave equation in inhomogeneous media

Su Chen¹ | Yi Ding¹ | Hiroe Miyake³ | Xiaojun Li^{1,2}

¹Key Laboratory of Urban Security and Disaster Engineering of the Ministry of Education, Beijing University of Technology, Beijing, China

²Institute of Geophysics, China Earthquake Administration, Beijing, China

³Earthquake Research Institute, University of Tokyo, Tokyo, Japan

Correspondence

Yi Ding, Key Laboratory of Urban Security and Disaster Engineering of the Ministry of Education, Beijing University of Technology, Beijing, 100124, China

Email: dingyi18@mails.ucas.edu.cn

Abstract

In scientific machine learning, the task of identifying partial differential equations accurately from sparse and noisy data poses a significant challenge. Current sparse regression methods may identify inaccurate equations on sparse and noisy datasets and are not suitable for varying coefficients. To address this issue, we propose a hybrid framework that combines two alternating direction optimization phases: discovery and embedding. The discovery phase employs current well-developed sparse regression techniques to preliminarily identify governing equations from observations. The embedding phase implements a recurrent convolutional neural network (RCNN), enabling efficient processes for time-space iterations involved in discretized forms of wave equation. The RCNN model further optimizes the imperfect sparse regression results to obtain more accurate functional terms and coefficients. Through alternating update of discovery-embedding phases, essential physical equations can be robustly identified from noisy and low-resolution measurements. To assess the performance of proposed framework, numerical experiments are conducted on various scenarios involving wave equation in elastic/viscoelastic and homogeneous/inhomogeneous media. The results demonstrate that the proposed method exhibits excellent robustness and accuracy, even when faced with high levels of noise and limited data availability in both spatial and temporal domains.

KEYWORDS

Discovery of wave equation, Sparse regression, System identification, Recurrent convolutional neural network, Discrete representation learning

1 | INTRODUCTION

Extracting partial differential equations (PDEs) from measurement data remains critical for modeling, simulation, and understanding the dynamical patterns and complex spatiotemporal behaviors in nature^{1,2}. Although our physical observations can often be described by derived physical laws, such as the wave equation, there are cases where the observed data do not conform to these laws or have not yet been described physically. Modern statistics and machine learning techniques use laws in data to discover plausible, simple, and explainable equations, learning to characterize representations of systems.

Recently, thanks to the advances in observational datasets and the thriving machine-learning community, there has been significant progress in distilling physical laws and governing equations from data^{3,4}. Current methods are mainly divided into closed and expandable library methods based on the library construction method. Expandable library methods do not need to predetermine an overcomplete library, they only need a randomly generated incomplete initial library to generate various unknown combinations by introducing methods such as genetic algorithms^{5,6,7}. Cheng and Alkhalifah^{8,9} combine neural networks and genetic algorithms for discovering the acoustic wave equation. One of the most popular closed library approaches for identifying physical laws is sparse identification of nonlinear Dynamics (SINDy)¹⁰, which introduces sparse linear regression into the discovery of parsimonious governing equations from a library of predefined candidate functions. Since then, the technique of sparse linear regression has drawn tremendous attention in the past few years, leading to variant applications across a range of scientific disciplines^{11,12,13}. Moreover, the sparsity-promoting paradigm, such as Sequential

Threshold Ridge regression (STRidge), has been expanded to encompass more general PDE discovery. This involves augmenting the library of candidate functions by incorporating spatial partial derivative terms¹⁴.

While previous research endeavors have achieved considerable success in data-driven PDE discovery, the standard sparse representation-based methods may yield inaccurate results as sparsity and noise levels escalate, posing a significant challenge in numerous real-world applications. Recently, several studies have made efforts to discover PDEs from noisy^{15,16,17} as well as sparse observations^{18,19}. On the other hand, sparse regression can only provide a scalar identification of the coefficients rendering it unsuitable for direct application in the inverse problem of varying spatial parameters.

Recent research on modeling physical systems using neural networks can be divided into two categories: continuous and discrete approaches. An typical work in continuous learning is the physics-informed neural networks based on fully connected neural networks²⁰, which have been used for forward^{21,22,23,24} and inverse^{25,26} analysis of wave equations. On the other hand, due to the lightweight architecture and hard-embedded characteristics of boundary conditions, physics-informed approaches based on convolutional neural network (CNN) have been used for PDE system modeling in discrete learning^{27,28,29}. However, due to limitations in computational efficiency³⁰ and spectral bias^{31,32}, learning the complex dynamics of wave propagation with neural networks remains challenging. Recently, by leveraging the inherent connection between temporal-spatial stepping processes and recurrent neural network (RNN) as well as convolutional layers (CLs), a recurrent convolutional neural network (RCNN) has been proposed for efficiently full-wave electromagnetic³³ modeling and mechanical wave modeling³⁴ on GPU platforms. The weight parameters in RCNN are directly derived from finite difference time domain (FDTD) formulas, enabling efficient processes for time-space iterations involved in discretized forms of PDEs.

We present a novel computational framework designed to unveil viscoelastic wave equation from sparse and noisy measurement data. Our framework combines sparse regression with an optimized RCNN model. The main contributions of this paper are three-fold:

1. We propose an alternating optimization discovery-embedding framework. Through sparse regression in the discovery phase, we identify essential equation terms and establish reasonable initial coefficients. Subsequently, the RCNN model in the embedding phase can filter equation terms and optimize coefficients, refining the discovered system further.
2. By utilizing the inherent connection between the time-marching process and RNN, we established a conceptual comparison between viscoelastic wave physics system and standard RNN.
3. We use a series of convolution kernels (filters) in CLs to approximate the discretization scheme of finite difference (FD) operators. Different boundary conditions are embedded into the FD-based filters, including homogeneous Dirichlet, Neumann, and absorbing boundary conditions.

To convey this idea, we structure the rest of this paper as follows. The problem statement is defined in Section 2.1. The concept of sparse regression and the limitations of its application are discussed in Section 2.2. In Section 2.3, we introduced the theory and optimization details of the RCNN model. Section 2.4 describes different boundary conditions embedded in the RCNN model. In Section 3, we implement a number of numerical experiments and show the results to evaluate the performance of our proposed approach. Section 4 finally provides a discussion and concluding remarks.

2 | METHODOLOGY

2.1 | Problem statement

We aim to devise a learning paradigm to solve the inverse PDEs identification problem. In this work, we consider the general form of a wave equation consisting of:

$$u_{tt} = \mathcal{F} [u, u^2, \dots, \nabla_x u, \nabla_x^2 u, \nabla_x u \cdot u, \dots, u_t, \nabla_x u \cdot u_t \dots], \quad (1)$$

where u_t, u_{tt} are the first and second-order temporal derivatives of the displacement $u(x, t)$. $\mathcal{F} [\cdot]$ is a composite function describing the right-hand side (RHS) of PDEs, which involving combinations of u and its spatial or temporal derivatives.

Our objective is to identify the closed form of $\mathcal{F} [\cdot]$ from available spatiotemporal measurements which are assumed to be incomplete, scarce, and noisy commonly seen in real-world applications. The task of identifying function $\mathcal{F} [\cdot]$ comprises two components. It involves the identification of suitable functional terms from an overcomplete candidate library. Secondly, it

entails the determination of the corresponding nonzero coefficient vector, which may exhibit spatial variations, owing to the heterogeneity of the Earth's media. Fortunately, there exists a parsimonious form for canonical PDEs (including the wave equation), wherein the RHS has only a limited number of terms in an active state.

We consider a one-dimensional (1D) wave equation containing a viscous term as shown in the following equation³⁵:

$$\frac{\partial^2 u}{\partial t^2} = c^2 \frac{\partial^2 u}{\partial x^2} + \eta \frac{\partial u}{\partial t}, \quad (2)$$

where we assume that the body force is absent, c is the spatially varying wave velocity, η is defined as the viscous factor. The wavefield is excited by Ricker wavelet distributed in space at $t = 0$:

$$R(x) = (2(\pi f_0(x - 1/f_0))^2 - 1) \cdot \exp(-\pi^2 f_0^2(x - 1/f_0)^2), \quad (3)$$

where f_0 is the central frequency. Due to the presence of time derivative terms in the viscous term, different viscoelastic wave equations result in different time-marching formulas, thereby significantly increasing the complexity of the problem. For simplicity, this paper focuses solely on viscoelastic wave equation of the form given by Eq. (2), assuming that the known right-hand side includes the u_t term, but the viscous factor η is unknown.

2.2 | Sparse Discovery

Here, we review the fundamentals of the partial differential equation functional identification of nonlinear dynamics (PDE-FIND) algorithm. PDE-FIND is similar to SINDy but with the library including partial derivatives.

Let us consider the observations $u_m \in \mathbb{R}^{n'_t \times n'_x}$ over n'_t time points and n'_x spatial locations on a coarse grid. Upon flattening u_m into a column vector $\mathbf{U} \in \mathbb{R}^{n'_t \cdot n'_x \times 1}$, it is possible to establish a library $\Theta(\mathbf{U}) \in \mathbb{R}^{n'_t \cdot n'_x \times D}$ consisting of D candidate functional terms,

$$\Theta(\mathbf{U}) = [u, u^2, \dots, \nabla_x u, \nabla_x^2 u, \nabla_x u \cdot u, \dots, u_t, \nabla_x u \cdot u_t \dots]. \quad (4)$$

Each column of the library $\Theta(\mathbf{U})$ corresponds to a particular candidate term of the governing equation, as shown in Fig. 1. The evolution of the PDE can be represented in this library as follows:

$$\mathbf{U}_t = \Theta(\mathbf{U})\Xi, \quad (5)$$

where $\Xi = \{\xi_1, \xi_2, \dots, \xi_D\} \in \mathbb{R}^{D \times 1}$ is the coefficient vector, and each non-zero term in Ξ corresponds to a term in the PDE. The requirement of sparse discovery is that each coefficient in Ξ is a scalar value.

However, due to the heterogeneity of the medium, the coefficients in Ξ should be spatially varying, i.e., $\Xi(x) = \{\xi_1(x), \xi_2(x), \dots, \xi_D(x)\}$, which will be further optimized in the embedding phase. Specifically, sparse regression provides reasonable functional terms and scalar initial coefficients for further optimization of the subsequent RCNN model. The schematic diagram of our proposed framework is illustrated in Fig. 1. Theoretical support for the RCNN model in embedding phase can be found in Section 2.3.

We assume that a sufficiently complete function library implies that all functional forms of the representation are fully contained in it. Given a library of candidate function $\Theta(\mathbf{U})$, sparse regression aims to find a suitable coefficient vector such that it satisfies the sparsity requirement and has a small regression error. To effectively discover the physical laws of a system, the resulting model must be easy to interpret. This means that the solution of library $\Theta(\mathbf{U})$ should contain only a finite number of terms in the final discovered model. To do this, various techniques and methods can be utilized to promote sparsity of the coefficient vector Ξ , such as least absolute shrinkage and selection operator (LASSO)³⁶, sequential thresholded least-squares (STLS)¹⁰, etc. In this study, it is achieved by using the sequential threshold ridge regression (STRidge) algorithm¹⁴ to solve the optimization problem described as

$$\hat{\Xi} = \arg \min_{\Xi} \{ \|\mathbf{U}_t - \Theta(\mathbf{U})\Xi\|_2 + \gamma \|\Xi\|_2 \}, \quad (6)$$

where $\|\Xi\|_2$ measures the sparsity of the coefficient vector, $\|\mathbf{U}_t - \Theta(\mathbf{U})\Xi\|_2$ denotes the regression error, γ is the coefficient that balances the sparsity and regression error, and Pareto analysis is used to choose the appropriate γ to get the appropriate result^{14,37}.

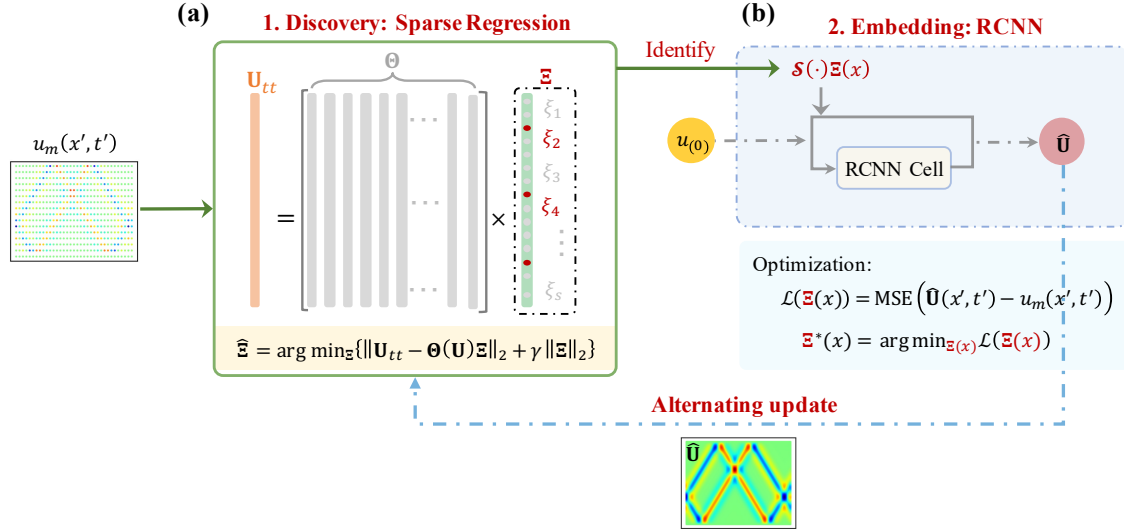


FIGURE 1 Schematic diagram of the proposed framework. (a) Discovery phase preliminarily identifies governing equations from observations. (b) Embedding phase use the RCNN model further optimizes the the imperfect function terms $\mathcal{S}(\cdot)$ and coefficients $\Xi(x)$ identified from discovery pahse. Given the measurements $u_m(x', t') \in \mathbb{R}^{n'_t \times n'_x}$ on a coarse grid (with resolution $n'_t \times n'_x$), RCNN model can provide the discovered equation, inverted coefficients (c and η), and high-resolution wavefield prediction $\hat{U} \in \mathbb{R}^{n_t \times n_x}$. The alternating update strategy implies that the high-resolution wavefield predicted by RCNN are provided to the discovery phase.

2.3 | Recurrent convolutional neural network

2.3.1 | Time-marching scheme in RNN

Here, we first established the conceptual comparison of viscoelastic wave physics system and a standard RNN³⁸. The connections between RNN nodes form a directed graph along the a temporal sequence, allowing RNN to model temporal dynamics. At a given time step t , an RNN operates on the current input vector $\mathbf{x}_{(t)}$ in the sequence and the previous hidden state vector $\mathbf{h}_{(t-1)}$ to produce an output vector $\mathbf{y}_{(t)}$ and an updated hidden state $\mathbf{h}_{(t)}$, which can be described by the following update equation,

$$\begin{aligned} \mathbf{h}_{(t)} &= \sigma^{(h)}(\mathbf{W}_{hh} \cdot \mathbf{h}_{(t-1)} + \mathbf{W}_{xh} \cdot \mathbf{x}_{(t)}), \\ \mathbf{y}_{(t)} &= \sigma^{(y)}(\mathbf{W}_{yh} \cdot \mathbf{h}_{(t)}), \end{aligned} \quad (7)$$

where \mathbf{W}_{hh} , \mathbf{W}_{xh} , and \mathbf{W}_{yh} are dense matrices optimized during training. $\sigma^{(h)}$ and $\sigma^{(y)}$ are nonlinear activation functions. The hidden state \mathbf{h}_t at the current time step t will be involved in computing the hidden state \mathbf{h}_{t+1} at the next time step $t+1$. In the next time step, the definition of the hidden state is the same as that used in the previous time step, so the calculation in Eq. (7) is recurrent.

In each alternating update of the discovery-embedding cycle, we define the equation obtained using sparse regression in the discovery phase as,

$$u_{tt} = \mathcal{S}(u)\Xi(x) + \hat{\eta}u_t, \quad (8)$$

where $\mathcal{S}(\cdot)$ contains the spatially correlated PDE operators discovered by sparse regression, $\Xi(x)$ is the corresponding coefficient matrix discovered. $\mathcal{S}(u)\Xi(x)$ represents one or more terms in the PDE obtained by multiplying function terms with corresponding coefficients and accumulating them. Note that $\hat{\eta}$ is the coefficient in $\Xi(x)$ corresponding to u_t in the discovery phase. For simplicity, we extract $\hat{\eta}$ from $\Xi(x)$ and express it explicitly here.

Using a time increment of δt to discretize Eq. (8) with finite difference scheme, we obtain the recursive relation

$$\frac{u_{(t+1)} - 2u_{(t)} + u_{(t-1)}}{\delta t^2} = \mathcal{S}(u_{(t)})\Xi(x) + \hat{\eta} \frac{u_{(t+1)} - u_{(t-1)}}{2\delta t}. \quad (9)$$

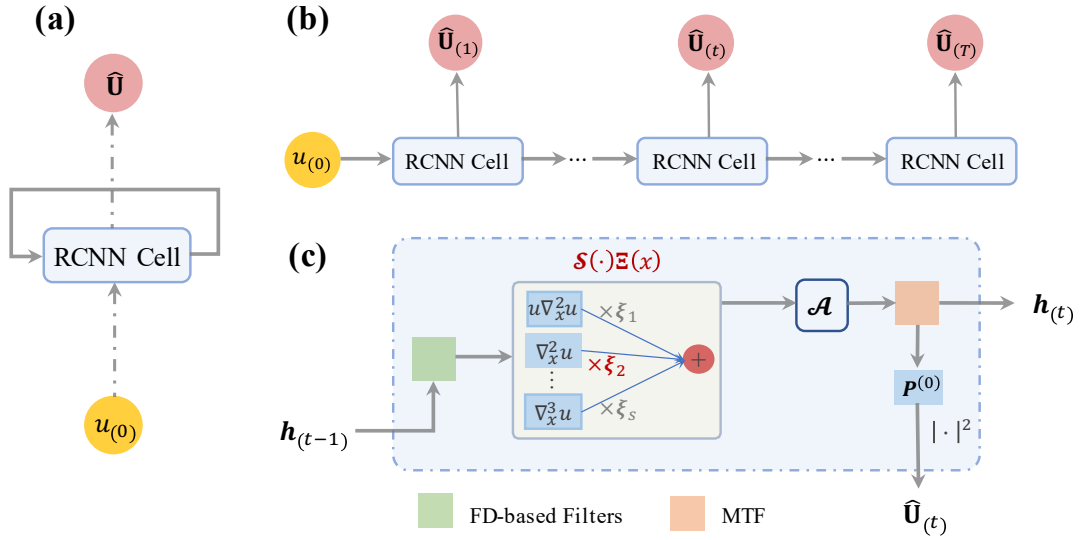


FIGURE 2 The architecture of RCNN model in embedding phase. (a) The directed acyclic graph of a RCNN for the forward modelling. (b) The unrolled directed acyclic graph of the RCNN. $\hat{\mathbf{U}}_{(1)}$ and $\hat{\mathbf{U}}_{(T)}$ are the predicted wavefield of the RCNN cell at times t_1 and t_T , respectively. (c) The single RCNN cell architecture. $\mathcal{S}(\cdot)\Xi(x)$ is provided by the sparse regression from the previous discovery phase.

The above equation can be written in matrix form

$$\begin{bmatrix} u_{(t+1)} \\ u_{(t)} \end{bmatrix} = \begin{bmatrix} \frac{4+2\delta t^2 \mathcal{S}(\cdot)\Xi(x)}{2-\tilde{\eta}\delta t} & -\frac{2+\tilde{\eta}\delta t}{2-\tilde{\eta}\delta t} \\ 1 & 0 \end{bmatrix} \cdot \begin{bmatrix} u_{(t)} \\ u_{(t-1)} \end{bmatrix}. \quad (10)$$

To relate Eq. (10) to the RNN update equation in Eq. (7), we define

$$\mathcal{A} = \begin{bmatrix} \frac{4+2\delta t^2 \mathcal{S}(\cdot)\Xi(x)}{2-\tilde{\eta}\delta t} & -\frac{2+\tilde{\eta}\delta t}{2-\tilde{\eta}\delta t} \\ 1 & 0 \end{bmatrix}. \quad (11)$$

The hidden state \mathbf{h}_t of the wave system is defined as the concatenation of the wavefields at time steps t and $t+1$, $\mathbf{h}_t \equiv [u_{(t+1)}, u_{(t)}]^T$. Then, the update equation for the discovered wave system defined by Eq. (8) can be rewritten as

$$\begin{aligned} \mathbf{h}_{(t)} &= \mathcal{A} \cdot \mathbf{h}_{(t-1)}, \\ \mathbf{U}_{(t)} &= |\mathbf{P}^{(o)} \cdot \mathbf{h}_{(t)}|^2, \end{aligned} \quad (12)$$

where $\mathbf{U}_{(t)}$ represents the measurement output at a fixed receiver position and time, corresponding to \mathbf{y}_t in Eq. (7). The connection between hidden state \mathbf{h}_t and outputs $\mathbf{U}_{(t)}$ in the wave RNN is defined by the linear operator $\mathbf{P}^{(o)}$, playing a similar role to the weight matrix $\mathbf{W}_{(yh)}$ in the output layer of standard RNN. According to Hughes et al.³⁸ definition, $\mathbf{P}^{(o)} \equiv [\mathbf{M}^{(o)T}, \mathbf{o}]$, where the linear operator $\mathbf{M}^{(o)}$ defines the corresponding spatial distribution of measurement points, and \mathbf{o} is a matrix of all zeros.

It is worth mentioning that, since sparse regression discovers the wave equation without source term from observations, the wave RNN described by Eq. (12) actually corresponds to a standard RNN with no input vector ($\mathbf{x}_{(t)}$ in Eq. (8)). In a standard RNN, \mathbf{W}_{hh} captures contributions from the previous state. It can be trained to learn how to use the hidden variables from previous time steps in the current time step. In contrast, in wave RNN, we leverage physical priors from FDTD by fixing \mathcal{A} as an untrainable matrix described by Eq. (11).

So far, we have shown that the time-marching scheme of the viscoelastic wave equation can be directly mapped to the framework of an RNN. Fig. 2 shows the architecture of the RCNN model at three levels of granularity.

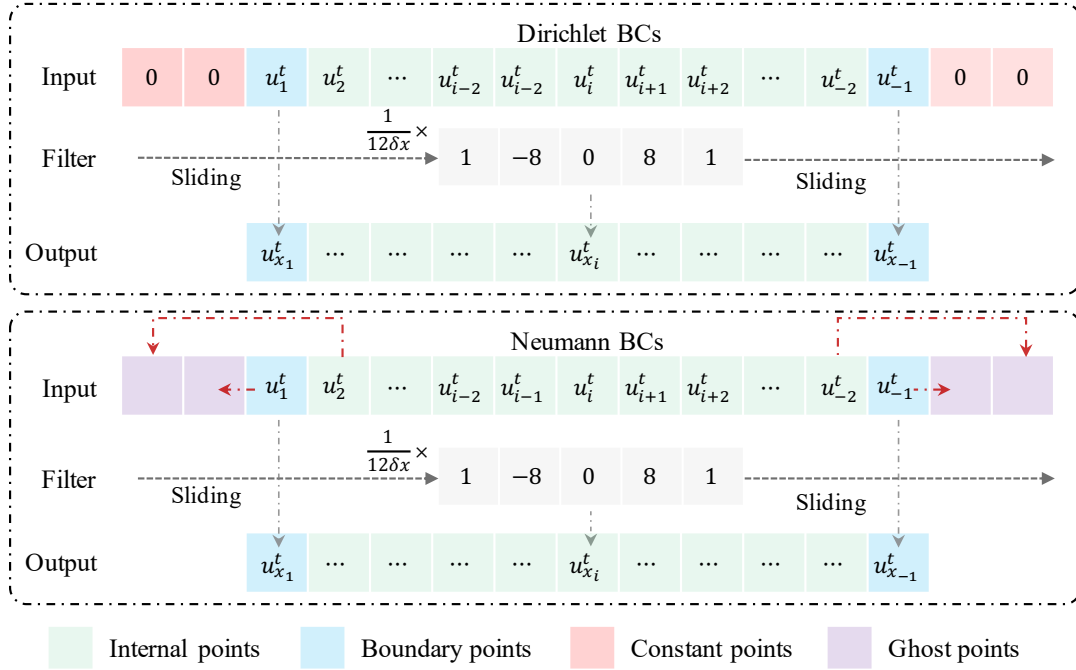


FIGURE 3 Schematic diagram of FD-based filters and hard embedding of boundary conditions. The filter $\mathcal{K}_x = \frac{1}{12\delta x}(1, -8, 0, 8, 1)$ implements a 4th-order FD derivative operation in 1D CNN. For fixed boundary condition (upper figure), directly fill constant 0 on the extended nodes outside the boundary. For free-surface boundary condition (lower figure), determine the filling values of ghost points based on the values of the internal wavefield.

2.3.2 | Finite difference-based filters in CNN

The efficacy of a classical numerical PDE solver relies on the translational similarity of its discretized local differential operators³⁹. From a machine learning perspective, these “translational similar” differential operators resemble the concept of convolution operators that function as the cornerstone to embed the “translational invariant” priors into neural networks⁴⁰.

Previous work investigated a deep relationship between convolutions and differentiations and discussed the connection between the order of the sum rules of the filters and the order of the differentiation operators^{41,42}. By utilizing the concept of “translation invariance” observed in PDE differential operators, we can approximate discretization schemes of finite difference operators using a series of convolution kernels in CLs.

For the 1D wave equation, we apply second-order and fourth-order central difference schemes separately in the temporal and spatial dimensions. A uniquely determined gradient-free “frozen” filter is implemented on an unbiased convolution layer. The receptive field is defined as the input region that each FD-based filter focuses on. In the temporal direction, the filter \mathcal{K}_t and receptive field $F(u_x^t)$ for implementing the first-order derivative using a three-point difference scheme are defined as:

$$F(u_x^t) = [u_x^{t-1}, u_x^t, u_x^{t+1}], \quad (13)$$

$$\mathcal{K}_t = (-1, 0, 1) \times \frac{1}{2\delta t},$$

where δt is the time interval. The receptive field $F(u_x^t)$ includes three adjacent temporal solution variables u . Then, the first-order time derivative of u can be expressed in CNN as:

$$\frac{\partial u_x^t}{\partial t} \approx \frac{1}{2\delta t}(-1, 0, 1) [u_x^{t-1}, u_x^t, u_x^{t+1}] = \mathcal{K}_t \cdot F(u_x^t). \quad (14)$$

Observing the above equation, it can be found that the dot product between the designed filter and the corresponding receptive field is equivalent to the FD derivative process. Differential in spatial dimension are consistent with time, but require more neighboring points to be involved in the differentiation process. Fig. 3 illustrates the derivative process of FD-based filters in 1D

CLs using \mathcal{K}_x as an example. The derivatives of each order in the spatial direction can be expressed as,

$$\begin{aligned}\frac{\partial u_{x_i}^t}{\partial x} &\approx \mathcal{K}_x \cdot F(u_{x_i}^t) = \frac{1}{12\delta x}(1, -8, 0, 8, 1) \cdot F(u_{x_i}^t), \\ \frac{\partial^2 u_{x_i}^t}{\partial x^2} &\approx \mathcal{K}_{xx} \cdot F(u_{x_i}^t) = \frac{1}{12\delta x^2}(-1, 16, -30, 16, -1) \cdot F(u_{x_i}^t), \\ \frac{\partial^3 u_{x_i}^t}{\partial x^3} &\approx \mathcal{K}_{xxx} \cdot F(u_{x_i}^t) = \frac{1}{12\delta x^3}(-1, 2, 0, -2, 1) \cdot F(u_{x_i}^t),\end{aligned}\quad (15)$$

where δx is the spatial mesh size. \mathcal{K}_x , \mathcal{K}_{xx} and \mathcal{K}_{xxx} denote the first three orders of filters corresponding to the five-point center difference scheme, respectively. The receptive field is composed of the solution variables from five spatially adjacent positions, denoted as $F(u_{x_i}^t) = [u_{x_{i-2}}^t, u_{x_{i-1}}^t, u_{x_i}^t, u_{x_{i+1}}^t, u_{x_{i+2}}^t]$.

2.3.3 | Optimization

Given the measurements $u_m(x', t') \in \mathbb{R}^{n'_t \times n'_x}$ on a coarse grid (with resolution $n'_t \times n'_x$), the embedding phase is optimized by minimizing the mean square error (MSE) between model predictions and coarse measurements. Specifically, the loss function of the RCNN model is defined as:

$$\mathcal{L}(\Xi(x)) = \text{MSE} \left(\hat{\mathbf{U}}(x', t') - u_m(x', t') \right), \quad (16)$$

where $\hat{\mathbf{U}}(x', t')$ denotes the mapping of the high-resolution prediction $\hat{\mathbf{U}}$ on the coarse grid (x', t') .

The training process of the parameterized RCNN is equivalent to searching for the optimal parameters in a function space, in order to learn governing equation of the dynamical system and achieve high-resolution prediction from observational data. Utilizing the coefficients corresponding to predetermined function terms from sparse regression as initial estimates, these trainable parameters are then optimized in the RCNN model:

$$\Xi^*(x) = \arg \min_{\Xi(x)} \{ \mathcal{L}(\Xi(x)) \}. \quad (17)$$

We optimize the RCNN model using an Adam optimizer with a stochastic gradient descent method⁴³ followed by optimization with the L-BFGS optimizer⁴⁴. Training with the L-BFGS optimizer stops when the maximum number of iterations is reached or convergence is achieved. We mainly use the Adam optimizer to provide a good starting point for L-BFGS and to speed up the training process. We added a filtering mechanism for the RNN cell, and if the average value of any item in $\Xi(x)$ during optimization is less than 10^{-3} , the corresponding item is removed from the library. We add a filtering mechanism to the RNN cell such that if the average value of any term in $\Xi(x)$ is less than 10^{-3} during the optimization process, the corresponding term will be removed from the discovered equation.

Furthermore, we introduce a alternating update strategy that effectively enhances recognition efficiency and accuracy for the case of homogeneous media. Specifically, we first utilize sparse regression to identify the initial equation from sparse and noisy data $u_m(x', t')$. Then employ Adam and L-BFGS optimizers in RCNN model to provide clean high-resolution results $\hat{\mathbf{U}}(x, t)$ for the next cycle of sparse regression.

2.4 | Boundary conditions setting

The boundary condition $u = 0$ in a wave equation reflects the wave, but u changes sign at the boundary, while the condition $u_x = 0$ reflects the wave as a mirror and preserves the sign, called the homogeneous Dirichlet or Neumann conditions, respectively. For simulation problems involving the free surface, the implementation of the boundary condition is crucial, i.e., satisfying $\frac{\partial u}{\partial \mathbf{n}} \equiv \mathbf{n} \cdot \nabla u = 0$, where the derivative $\partial/\partial \mathbf{n}$ is in the outward normal direction from a general boundary. For a 1D domain $[0, L]$, we have that $\frac{\partial u}{\partial \mathbf{n}}|_{x=L} = \frac{\partial u}{\partial x} = 0$.

For homogeneous Dirichlet BCs, it can be strictly incorporated into the solution variables through time-invariant padding operation. For homogeneous Neumann BCs, we extended the mesh using ghost points⁴⁵, and derived the padding values of the ghost points based on the 1D free-surface boundary condition $u_x = 0$. In this way, applying the standard difference scheme at the boundary point will be correct and will ensure that the solution is compatible with the boundary conditions. Fig. 3 shows the details of applying homogeneous Dirichlet and Neumann boundary conditions in 1D CNN.

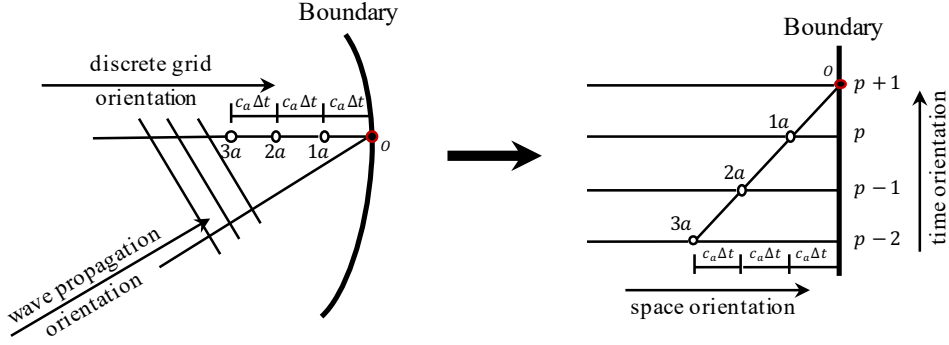


FIGURE 4 Schematic diagram of multi-transmitting formula (MTF).

We consider the problem of identifying and inverting the wave equation in energy-closed systems versus energy-open systems with simulated real subsurface half-space. For wave simulation of energy-open system, absorbing boundary conditions (ABCs) are typically needed to prevent spurious wave reflections at the boundaries. In this paper, we employ the multi-transmitting formula (MTF) to satisfy the transmission of outgoing waves at the bottom boundary^{46,47,48}. In MTF, the motion of an arbitrary artificial boundary node at each timestep is directly predicted from the motions of some adjacent nodes at several previous timesteps. It is expressed by a discrete formula as

$$u_0^{p+1} = \sum_{j=1}^N (-1)^{j+1} C_j^N u_{ja}^{p+1-j}, \quad (18)$$

where N is the transmitting order and $C_j^N = N!/(j!(N-j)!)$ are binomial coefficients. $u_0^{p+1} = u(0, (p+1)\delta t)$ denotes the motion of artificial boundary node 0 at time instant $(p+1)\delta t$, as shown in Fig. 4. $u_{ja}^{p+1-j} = u(jc_a\delta t, (p+1-j)\delta t)$ denotes the motion of a uniformly distributed node ja on a discrete grid line pointing from point 0 to the inner domain at the moment $(p+1-j)\delta t$. c_a is a user-defined hyperparameter called artificial wave velocity.

The formula of MTF yields to $u_0^{p+1} = u_{1a}^p$ for $N = 1$, $u_0^{p+1} = 2u_{1a}^p - u_{2a}^{p-1}$ for $N = 2$, and $u_0^{p+1} = 3u_{1a}^p - 3u_{2a}^{p-1} + u_{3a}^{p-2}$ for $N = 3$. The MTF is combined with the inner-domain discrete format by interpolating the motion of each MTF computation point $1a, 2a, \dots, Na$ with the motion of nearby inner-domain nodes. This interpolation is easy to implement and offers multiple selectable options. In this work, we adopt the 2nd order MTF ($N = 2$) numerical scheme with quadratic interpolation⁴⁹.

3 | NUMERICAL EXPERIMENTS

In this section, we validate the performance of our proposed method with some numerical results of potential practical significance, considering wave propagation in elastic/viscoelastic, homogeneous/inhomogeneous media.

We utilize the finite difference method (FDM) to generate datasets, employing both second-order central difference scheme and fourth-order central difference scheme for temporal and spatial discretization. The number of grid points in the discrete spatial domain is 128, and the number of discrete points in the temporal domain is determined by the Courant–Friedrichs–Lewy (CFL) condition. To ensure the stability of the finite difference method, we set the time interval to $\delta t = 0.9\delta x/\sqrt{c}$.

As mentioned in Section 2.1, we assume that the viscosity is controlled by the u_t term in all cases of this work. Moreover, during the sparse regression phase, the viscous term will be exempted from filtering. In the first identification, η is set to 0.1 as the initial value for inversion. The learning rate of the Adam optimizer of RCNN model is initialized to $5e^{-3}$.

To quantitatively evaluate the performance of the proposed method, two types of relative \mathcal{L}_2 errors are defined in terms of the wavefield and wave velocity. Across all cases, the relative \mathcal{L}_2 error of the wavefield, defined as $\epsilon(\mathbf{U}) = \|\hat{\mathbf{U}} - \mathbf{U}_{\text{true}}\|_2 / \|\mathbf{U}_{\text{true}}\|$, measures the relative distance between the predicted wavefield $\hat{\mathbf{U}}$ and the ground truth \mathbf{U}_{true} . On the other hand, the relative \mathcal{L}_2 error of the wave velocity $\epsilon(c) = \|\hat{c} - c_{\text{true}}\|_2 / \|c_{\text{true}}\|$ represents the difference between the inverted wave velocity \hat{c} and the exact wave velocity c_{true} in heterogeneous media.

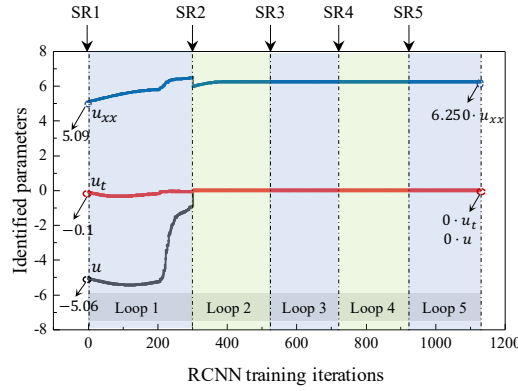


FIGURE 5 Case 1: Discovery-embedding alternately updates the identified function terms and corresponding coefficients. In the first execution of sparse regression (SR1), the discovered equation is $u_{tt} = 5.09u_{xx} - 5.06u - 0.1u_t$. After the fifth loop (Loop 5), the correct equation $u_{tt} = 6.25u_{xx}$ is obtained.

3.1 | Wave equation in an elastic homogeneous medium

We first consider two cases of wave propagation in elastic homogeneous media. In Case 1, the reflection phenomenon of wave propagation in a energy-closed system is modeled by imposing homogeneous Dirichlet boundary conditions at both ends of the spatial medium. In Case 2, we impose a homogeneous Neumann boundary condition $u_x = 0$ at the top of the medium ($x = L$) and MTF at the bottom of the medium to simulate wave propagation in a 1D half-space. The finite difference method is used to solve Eq. (1) and generate synthetic data. In this case, the spatial range is $x \in [0, 6]$, the temporal range is $t \in [0, 5]$, the wave velocity c is 2.5. The number of grid points in the spatial domain is 128 and the time domain is discretized into 420 uniform points. The source is represented by the initial distribution of the Ricker wavelet on x , with a central frequency of $f_0 = 0.5$.

We performed downsampling on the wavefield in both spatial and temporal dimensions, with downsampling factors of 8 and 12 respectively. This results in a measurement resolution of only 16×35 provided to the sparse regression algorithm, accounting for 1.04% of the synthetic dataset. The candidate functions in the function library are designed to capture the different forms of wave equations that may appear in the measurement. We employ a dictionary denoted as $\Theta(\mathbf{U}) \in \mathbb{R}^{35 \times 16 \times 60}$, which contains 60 candidate functions. These candidate functions are constructed to include polynomial terms up to the third order $\{1, u, u^2, u^3\}$ and derivatives up to the third order $\{1, u_x, u_x^2, u_{xx}, u_{xx}^2, u_{xxx}, u_{xxx}^2, u_t\}$, as well as combinations of them.

Due to the extremely sparse wavefield measurement, the initial sparse regression provides inaccurate results for both two cases, as shown in Figs. 5 and 6. For Case 1, the identified equation after initial sparse regression is $u_{tt} = 5.09u_{xx} - 5.06u - 0.1u_t$, and $u_{tt} = 5.45u_{xx} - 4.38u - 0.1u_t$. However, in the subsequent RCNN optimization, the coefficients corresponding to the erroneous terms u and u_t gradually approach zero. We executed a total of 5 loops for Case 1 and 4 loops for Case 2. In each of loop we first performed sparse regression, followed by 200 epochs of training using the Adam optimizer. The L-BFGS was used by up to 100 epochs of optimization, as the L-BFGS optimizer may stop early. From the sparse regression of the second loop, the correct function terms are obtained. In the following iterations, the coefficients are fine-tuned, resulting in highly accurate equations. Once the training is completed, a high-resolution solution can be inferred from the trained model, as shown in Fig. 7.

3.2 | Case 3: viscoelastic wave equation in a homogeneous medium

In the development of the Cases 1 and 2, a perfectly elastic medium was considered. For studies where small deformations occur, many elastic materials do not deviate grossly from perfectly elastic behavior. It is well-known, however, that when materials are set in vibration, the vibrations are accompanied by dissipation, due to the conversions of elastic energy to internal energy⁵⁰. In Case 3, we consider the wave equation in a viscoelastic, homogeneous and energy-closed system. In this case, the spatial range is $x \in [0, 3]$, the temporal range is $t \in [0, 3]$, and we set $c = 1.2$, $\eta = -1.0$. The number of grid points in the spatial domain is 128 and the time domain is discretized into 242 uniform points. The source is represented by the initial distribution of the Ricker wavelet on x , with a central frequency of $f_0 = 1.0$.

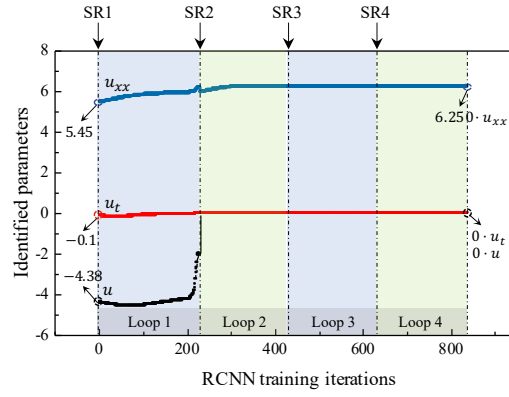


FIGURE 6 Case 2: Discovery-embedding alternately updates the identified function terms and corresponding coefficients. In the first execution of sparse regression (SR1), the discovered equation is $u_{tt} = 5.45u_{xx} - 4.38u - 0.1u_t$. The RCNN model in the fourth loop (Loop 4) outputs the correct equation $u_{tt} = 6.25u_{xx}$.

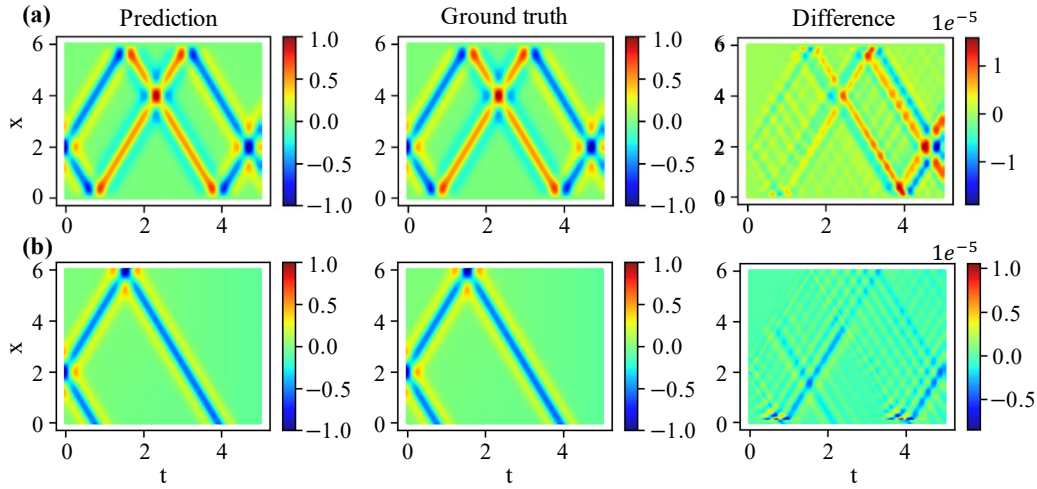


FIGURE 7 Comparison between predicted wavefield and ground truth. (a) Case 1. (b) Case 2.

We downsample the wavefield in the spatial and temporal dimensions with reduction factors of 8 and 12, respectively. This results in a wavefield data size of only 16×21 , which accounts for a mere 1.08% of the synthetic dataset. As in Case 1 and Case 2, we construct a dictionary representation as $\Theta(\mathbf{U}) \in \mathbb{R}^{21 \cdot 16 \times 60}$, which contains 60 candidate functions.

Fig. 8 illustrates the progressive evolution of identified coefficients during five loops, with each loop utilizing a fixed Adam setting of 200 epochs. The initial outcome yielded by the sparse regression technique is $u_{tt} = 1.246u_{xx} - 0.1u_t$, disclosing imprecise wave velocity and viscosity coefficients attributed to the limited number of measurements available. However, significantly improved outcomes are achieved following the RCNN optimization in the first loop. Moving on to Fig. 9, a comparative analysis is presented, where the predicted wavefield generated by our method is contrasted against results obtained using finite difference method, accompanied by their respective errors. Evidently, our method adeptly captures the phenomenon of wave attenuation in viscoelastic media.

3.3 | Case 4: viscoelastic wave equation with linearly varying wave velocity

In this subsection, we illustrate the performance of the proposed method in terms of the viscoelastic wave equation with linearly varying wave velocity. Homogeneous Dirichlet boundary conditions are imposed at both ends of the spatial medium and wave

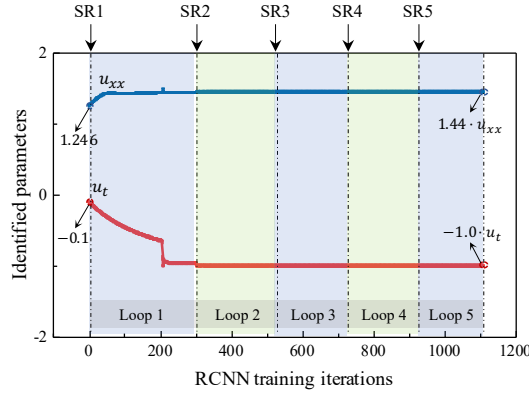


FIGURE 8 Case 3: Discovery-embedding alternately updates the identified function terms and corresponding coefficients. In the first execution of sparse regression (SR1), the discovered equation is $u_{tt} = 1.246u_{xx} - 0.1u_t$. After the fifth loop (Loop 5), the correct equation $u_{tt} = 1.44u_{xx} - 1.0u_t$ is obtained.

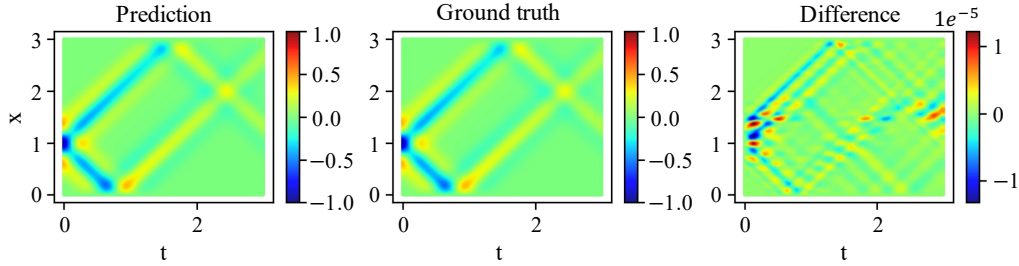


FIGURE 9 Comparison between the predicted wavefield and ground truth in Case 3.

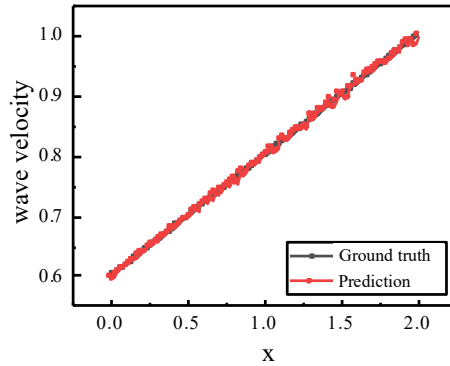


FIGURE 10 Comparison between the inverted wave velocity model and the ground truth.

energy attenuation is considered simultaneously. The model is specifically set up with $x \in [0, 2]$, $t \in [0, 3]$, $\eta = -0.5$, and the wave velocity was set to vary linearly from 0.6 to 1.0. The central frequency f_0 of Ricker source is 1.5. The number of grid points in the spatial domain is 128 and the time domain is discretized into 302 uniform points.

The observations provided to sparse regression and RCNN training were downsampled to a coarse grid of 26×31 , which represents only 2.09% of the synthesized dataset. The candidate function library is the same as in the previous case, i.e., $\Theta(\mathbf{U}) \in \mathbb{R}^{31 \cdot 26 \times 60}$. Although RCNN phase provides high-resolution measurements, the inherent limitations of sparse regression result in only being able to identify scalar wave velocity in each cycle. Therefore, the cycle training strategy mentioned in Section

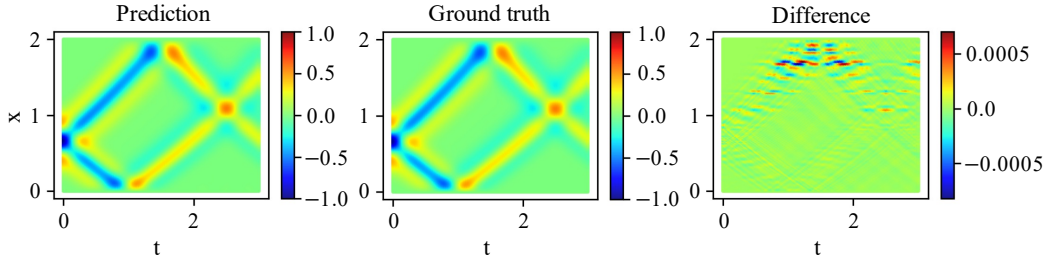


FIGURE 11 Comparison between the predicted wavefield and ground truth in Case 4.

2.3.3 was not employed in Case 4. At the beginning, sparse regression identified a scalar wave velocity of 0.739, which was used as an initial value for the RCNN optimization. We performed optimization on RCNN by employing the Adam optimizer for a total of 1000 epochs. Following that, we proceeded with additional optimization using L-BFGS for a maximum of 500 epochs.

The comparison between the predicted wave velocities and the true wave velocities is shown in Fig. 10. It can be observed that the predicted wave velocities of the model closely match the true values. Furthermore, our method accurately identified the viscous factor, $\eta = -0.499926$, directly from the observed data. The optimized model is capable of directly predicting high-resolution (128×302) wavefield. As shown in Figure 11, the predicted wavefield accurately captures variations in wave velocity and energy dissipation, exhibiting small point-wise errors when compared to the ground truth.

3.4 | Ablation study

Next, we consider a more practical scenario where the data is disturbed by noise. For this purpose, the previously generated synthetic data was added with up to 20% noise. The identified RHS at different noise levels as well as the relative \mathcal{L}_2 errors of the wavefield ($\epsilon(\mathbf{U})$) in Cases 1-3 are shown in Table 1. For Case 4, the relative \mathcal{L}_2 errors of the predicted wavefield ($\epsilon(\mathbf{U})$) and the inverted wave velocity $\epsilon(c)$, as well as identified η by the proposed framework at different noise levels η are shown in Table 2.

It can be observed that the increase in noise level leads to inaccurate wave velocity identification and an increase in $\epsilon(\mathbf{U})$. Nevertheless, the proposed method is able to successfully identify viscoelastic wave equation and velocity model even in the presence of a large amount of noise.

TABLE 1 Performance of the proposed method in the case of homogeneous media.

Cases	Metrics	Noise Level					
		0%	0%	5%	10%	15%	20%
Case 1	RHS	$6.25019u_{xx}$	$6.24891u_{xx}$	$6.24895u_{xx}$	$6.24202u_{xx}$	$6.23343u_{xx}$	$6.22114u_{xx}$
	$\epsilon(\mathbf{U})$	$2.509e^{-5}$	$2.846e^{-3}$	$1.793e^{-3}$	$1.921e^{-2}$	$2.794e^{-2}$	$3.711e^{-2}$
Case 2	RHS	$6.24989u_{xx}$	$6.251659u_{xx}$	$6.25494u_{xx}$	$6.26064u_{xx}$	$6.26668u_{xx}$	$6.3061u_{xx}$
	$\epsilon(\mathbf{U})$	$5.178e^{-6}$	$3.652e^{-3}$	$9.652e^{-3}$	$1.7724e^{-2}$	$2.5986e^{-2}$	$4.166e^{-2}$
Case 3	RHS	$1.44004u_{xx}$	$1.44252u_{xx}$	$1.43774u_{xx}$	$1.43784u_{xx}$	$1.36802u_{xx}$	$1.34835u_{xx}$
	$\epsilon(\mathbf{U})$	$-1.0001u_t$	$-0.9729u_t$	$-0.9738u_t$	$-0.9678u_t$	$-0.9488u_t$	$-0.9226u_t$
		$1.603e^{-5}$	$1.832e^{-3}$	$9.289e^{-2}$	$4.723e^{-2}$	$8.228e^{-2}$	$5.514e^{-2}$

TABLE 2 Performance of the proposed method in the case of inhomogeneous media.

Case	Metrics	Noise Level					
		0%	0%	5%	10%	15%	20%
Case 4	η	-0.4999	-0.4922	-0.4926	-0.4904	-0.4801	-0.4726
	$\epsilon(c)$	$9.410e^{-3}$	$2.431e^{-2}$	$3.642e^{-2}$	$3.918e^{-2}$	$4.323e^{-2}$	$3.166e^{-1}$
	$\epsilon(\mathbf{U})$	$2.418e^{-4}$	$4.151e^{-3}$	$8.869e^{-2}$	$1.642e^{-2}$	$2.476e^{-2}$	$2.059e^{-1}$

4 | CONCLUSION AND DISCUSSION

We proposed a hybrid framework for the discovery and inversion of viscoelastic wave equation in inhomogeneous media, which couples the sparse regression technique and well-designed RCNN model. Our innovative paradigm leverages the manifold of priors derived from the techniques of discovering hidden PDEs from sparse data, the computational efficiency of numerical solvers, and well-established optimization tools. The proposed coupling scheme allows for the refinement of both the structure and coefficients of partial differential equations discovered through sparse regression. As a result, the constraint of scalar coefficients identified by previous sparse discovery methods is overcome, enabling successful identification and inversion of wave propagation in heterogeneous media. In summary, we have presented an effective, interpretable, and flexible method for accurately and reliably discovering wave equations from imperfect, sparse, and noisy observational data.

Furthermore, in recent years, many researchers have utilized scientific machine learning (SciML) to embed PDEs into neural networks. However, the lack of governing equations can pose a challenge in practical scenarios. Our proposed hybrid approach holds the potential to pave the way for us to discover more meaningful governing equations in the real world using proposed framework. For instance, it can aid in directly uncovering unknown control equations and inverting the properties of media from seismic data obtained from experiments and observations. These equations can then be further integrated into emerging SciML methods using established knowledge embedding techniques. The cycle of knowledge discovery and knowledge embedding forms a closed-loop, which will be explored in future research.

AUTHOR CONTRIBUTIONS

Su Chen: Conceptualization, Investigation, Methodology, Writing-Review& Editing. **Yi Ding:** Methodology, Software, Visualization, Writing-Original Draft, WritingReview& Editing. **Hiroe Miyake:** Formal analysis, Supervision, Validation, Writing-Review& Editing. **Xiaojun Li:** Resources, Supervision, Writing-Review& Editing.

ACKNOWLEDGMENTS

The authors are grateful for the research funding provided by the National Natural Science Foundation of China (NSFC, Grant Nos. 52192675, U1839202).

FINANCIAL DISCLOSURE

None reported.

CONFLICT OF INTEREST

The authors declare no potential conflict of interests.

REFERENCES

- Xu H, Zeng J, Zhang D. Discovery of Partial Differential Equations from Highly Noisy and Sparse Data with Physics-Informed Information Criterion. *Research*. 2023;6:0147. doi: 10.34133/research.0147
- Yu R, Wang R. Learning Dynamical Systems from Data: An Introduction to Physics-Guided Deep Learning. *Proceedings of the National Academy of Sciences*. 2024;121(27):e2311808121. doi: 10.1073/pnas.2311808121
- Bongard J, Lipson H. Automated Reverse Engineering of Nonlinear Dynamical Systems. *Proceedings of the National Academy of Sciences*. 2007;104(24):9943-9948. doi: 10.1073/pnas.0609476104
- Schmidt M, Lipson H. Distilling Free-Form Natural Laws from Experimental Data. *Science*. 2009;324(5923):81-85. doi: 10.1126/science.1165893
- Xu H, Chang H, Zhang D. DLGA-PDE: Discovery of PDEs with Incomplete Candidate Library via Combination of Deep Learning and Genetic Algorithm. *Journal of Computational Physics*. 2020;418:109584. doi: 10.1016/j.jcp.2020.109584
- Chen Y, Luo Y, Liu Q, Xu H, Zhang D. Symbolic Genetic Algorithm for Discovering Open-Form Partial Differential Equations (SGA-PDE). *Physical Review Research*. 2022;4(2):023174. doi: 10.1103/PhysRevResearch.4.023174
- Makke N, Chawla S. Interpretable Scientific Discovery with Symbolic Regression: A Review. *Artificial Intelligence Review*. 2024;57(1):2. doi: 10.1007/s10462-023-10622-0

8. Cheng S, Alkhalifah T. Robust Data Driven Discovery of a Seismic Wave Equation. *Geophysical Journal International*. 2023;236(1):537–546. doi: 10.1093/gji/ggad446
9. Cheng S, Alkhalifah T. Discovery of Physically Interpretable Wave Equations. *arXiv preprint arXiv:2404.17971*. 2024.
10. Brunton SL, Proctor JL, Kutz JN. Discovering Governing Equations from Data by Sparse Identification of Nonlinear Dynamical Systems. *Proceedings of the National Academy of Sciences*. 2016;113(15):3932–3937. doi: 10.1073/pnas.1517384113
11. Loiseau JC, Noack BR, Brunton SL. Sparse Reduced-Order Modelling: Sensor-Based Dynamics to Full-State Estimation. *Journal of Fluid Mechanics*. 2018;844:459–490. doi: 10.1017/jfm.2018.147
12. Loiseau JC, Brunton SL. Constrained Sparse Galerkin Regression. *Journal of Fluid Mechanics*. 2018;838:42–67. doi: 10.1017/jfm.2017.823
13. Stender M, Oberst S, Hoffmann N. Recovery of Differential Equations from Impulse Response Time Series Data for Model Identification and Feature Extraction. *Vibration*. 2019;2(1):25–46. doi: 10.3390/vibration2010002
14. Rudy SH, Brunton SL, Proctor JL, Kutz JN. Data-Driven Discovery of Partial Differential Equations. *Science Advances*. 2017;3(4):e1602614. doi: 10.1126/sciadv.1602614
15. Messenger DA, Bortz DM. Weak SINDy for Partial Differential Equations. *Journal of Computational Physics*. 2021;443:110525. doi: 10.1016/j.jcp.2021.110525
16. Sashidhar D, Kutz JN. Bagging, Optimized Dynamic Mode Decomposition for Robust, Stable Forecasting with Spatial and Temporal Uncertainty Quantification. *Philosophical Transactions of the Royal Society A: Mathematical, Physical and Engineering Sciences*. 2022;380(2229):20210199. doi: 10.1098/rsta.2021.0199
17. Fasel U, Kutz JN, Brunton BW, Brunton SL. Ensemble-SINDy: Robust Sparse Model Discovery in the Low-Data, High-Noise Limit, with Active Learning and Control. *Proceedings of the Royal Society A: Mathematical, Physical and Engineering Sciences*. 2022;478(2260):20210904. doi: 10.1098/rspa.2021.0904
18. Chen Z, Liu Y, Sun H. Physics-Informed Learning of Governing Equations from Scarce Data. *Nature Communications*. 2021;12(1):6136. doi: 10.1038/s41467-021-26434-1
19. Sun F, Liu Y, Sun H. Physics-informed spline learning for nonlinear dynamics discovery. *arXiv preprint arXiv:2105.02368*. 2021.
20. Raissi M, Perdikaris P, Karniadakis G. Physics-Informed Neural Networks: A Deep Learning Framework for Solving Forward and Inverse Problems Involving Nonlinear Partial Differential Equations. *Journal of Computational Physics*. 2019;378:686–707. doi: 10.1016/j.jcp.2018.10.045
21. Song C, Alkhalifah T, Waheed UB. Solving the Frequency-Domain Acoustic VTI Wave Equation Using Physics-Informed Neural Networks. *Geophysical Journal International*. 2021;225(2):846–859. doi: 10.1093/gji/ggab010
22. Ding Y, Chen S, Li X, Wang S, Luan S, Sun H. Self-Adaptive Physics-Driven Deep Learning for Seismic Wave Modeling in Complex Topography. *Engineering Applications of Artificial Intelligence*. 2023;123:106425. doi: 10.1016/j.engappai.2023.106425
23. Ding Y, Chen S, Li X, Jin L, Luan S, Sun H. Physics-Constrained Neural Networks for Half-Space Seismic Wave Modeling. *Computers & Geosciences*. 2023;181:105477. doi: 10.1016/j.cageo.2023.105477
24. Ren P, Rao C, Chen S, Wang JX, Sun H, Liu Y. SeismicNet: Physics-informed Neural Networks for Seismic Wave Modeling in Semi-Infinite Domain. *Computer Physics Communications*. 2024;295:109010. doi: 10.1016/j.cpc.2023.109010
25. Rasht-Behesht M, Huber C, Shukla K, Karniadakis GE. Physics-Informed Neural Networks (PINNs) for Wave Propagation and Full Waveform Inversions. *Journal of Geophysical Research: Solid Earth*. 2022;127(5):e2021JB023120. doi: 10.1029/2021JB023120
26. Zhang Y, Zhu X, Gao J. Seismic Inversion Based on Acoustic Wave Equations Using Physics-Informed Neural Network. *IEEE Transactions on Geoscience and Remote Sensing*. 2023;61:1–11. doi: 10.1109/TGRS.2023.3236973
27. Gao H, Sun L, Wang JX. PhyGeoNet: Physics-informed Geometry-Adaptive Convolutional Neural Networks for Solving Parameterized Steady-State PDEs on Irregular Domain. *Journal of Computational Physics*. 2021;428:110079. doi: 10.1016/j.jcp.2020.110079
28. Qu J, Cai W, Zhao Y. Learning Time-Dependent PDEs with a Linear and Nonlinear Separate Convolutional Neural Network. *Journal of Computational Physics*. 2022;453:110928. doi: 10.1016/j.jcp.2021.110928
29. Ren P, Rao C, Liu Y, Wang JX, Sun H. PhyCRNet: Physics-informed Convolutional-Recurrent Network for Solving Spatiotemporal PDEs. *Computer Methods in Applied Mechanics and Engineering*. 2022;389:114399. doi: 10.1016/j.cma.2021.114399
30. McCreivy N, Hakim A. Weak baselines and reporting biases lead to overoptimism in machine learning for fluid-related partial differential equations. *arXiv preprint arXiv:2407.07218*. 2024.
31. Tancik M, Srinivasan P, Mildenhall B, et al. Fourier Features Let Networks Learn High Frequency Functions in Low Dimensional Domains. *Advances in Neural Information Processing Systems*. 2020;33:7537–7547.
32. Wang S, Wang H, Perdikaris P. On the Eigenvector Bias of Fourier Feature Networks: From Regression to Solving Multi-Scale PDEs with Physics-Informed Neural Networks. *Computer Methods in Applied Mechanics and Engineering*. 2021;384:113938. doi: 10.1016/j.cma.2021.113938
33. Guo L, Li M, Xu S, Yang F, Liu L. Electromagnetic Modeling Using an FDTD-Equivalent Recurrent Convolution Neural Network: Accurate Computing on a Deep Learning Framework. *IEEE Antennas and Propagation Magazine*. 2023;65(1):93–102. doi: 10.1109/MAP.2021.3127514
34. Ji D, Li C, Zhai C, Cao Z. An Efficient Platform for Numerical Modeling of Partial Differential Equations. *IEEE Transactions on Geoscience and Remote Sensing*. 2024;62:1–13. doi: 10.1109/TGRS.2024.3409620
35. Idriss IM, Seed HB. Seismic Response of Horizontal Soil Layers. *Journal of the Soil Mechanics and Foundations Division*. 1968;94(4):1003–1031. doi: 10.1061/JSFEAQ.0001163
36. Tibshirani R. Regression Shrinkage and Selection via the Lasso. *Journal of the Royal Statistical Society Series B: Statistical Methodology*. 1996;58(1):267–288. doi: 10.1111/j.2517-6161.1996.tb02080.x
37. Rao C, Ren P, Wang Q, Buyukozturk O, Sun H, Liu Y. Encoding Physics to Learn Reaction–Diffusion Processes. *Nature Machine Intelligence*. 2023;5(7):765–779. doi: 10.1038/s42256-023-00685-7
38. Hughes TW, Williamson IAD, Minkov M, Fan S. Wave Physics as an Analog Recurrent Neural Network. *Science Advances*. 2019;5(12):eaay6946. doi: 10.1126/sciadv.aay6946
39. Wu Z, He X, Li Y, et al. Neural Partial Differential Equations with Functional Convolution. *arXiv preprint arXiv:2303.07194*. 2023.
40. LeCun Y, Bengio Y. Convolutional Networks for Images, Speech, and Time Series. *The handbook of brain theory and neural networks*. 1995;3361(10):1995.
41. Cai JF, Dong B, Osher S, Shen Z. Image Restoration: Total Variation, Wavelet Frames, and Beyond. *Journal of the American Mathematical Society*. 2012;25(4):1033–1089. doi: 10.1090/S0894-0347-2012-00740-1

42. Dong B, Jiang Q, Shen Z. Image Restoration: Wavelet Frame Shrinkage, Nonlinear Evolution PDEs, and Beyond. *Multiscale Modeling & Simulation*. 2017;15(1):606–660. doi: 10.1137/15M1037457
43. Kingma DP. Adam: A method for stochastic optimization. *arXiv preprint arXiv:1412.6980*. 2014.
44. Liu DC, Nocedal J. On the Limited Memory BFGS Method for Large Scale Optimization. *Mathematical Programming*. 1989;45(1-3):503–528. doi: 10.1007/BF01589116
45. Wang S, Petersson NA. Fourth Order Finite Difference Methods for the Wave Equation with Mesh Refinement Interfaces. *SIAM Journal on Scientific Computing*. 2019;41(5):A3246–A3275. doi: 10.1137/18M1211465
46. Liao Z, Wong H. A Transmitting Boundary for the Numerical Simulation of Elastic Wave Propagation. *International Journal of Soil Dynamics and Earthquake Engineering*. 1984;3(4):174–183. doi: 10.1016/0261-7277(84)90033-0
47. Xing H, Li X, Li H, Xie Z, Chen S, Zhou Z. The Theory and New Unified Formulas of Displacement-Type Local Absorbing Boundary Conditions. *Bulletin of the Seismological Society of America*. 2021;111(2):801–824. doi: 10.1785/0120200155
48. Xing H, Li X, Li H, Liu A. Spectral-Element Formulation of Multi-Transmitting Formula and Its Accuracy and Stability in 1D and 2D Seismic Wave Modeling. *Soil Dynamics and Earthquake Engineering*. 2021;140:106218. doi: 10.1016/j.soildyn.2020.106218
49. Liao ZP, Liu JB. Numerical Instabilities of a Local Transmitting Boundary. *Earthquake Engineering & Structural Dynamics*. 1992;21(1):65–77. doi: 10.1002/eqe.4290210105
50. Charlier JP, Crowet F. Wave Equations in Linear Viscoelastic Materials. *The Journal of the Acoustical Society of America*. 1986;79(4):895–900. doi: 10.1121/1.393685

SUPPORTING INFORMATION

Additional supporting information may be found in the online version of the article at the publisher's website.